Robustness of sensory-evoked excitation is increased by inhibitory inputs to distal apical tuft dendrites

Robert Egger[a,b,c,1], Arno C. Schmitt[d,1], Damian J. Wallace[d,e], Bert Sakmann[f,2], Marcel Oberlaender[a,b,f,2], and Jason N. D. Kerr[d,e]

[a]Computational Neuroanatomy Group, Max Planck Institute for Biological Cybernetics, 72076 Tübingen, Germany; [b]Bernstein Center for Computational Neuroscience, 72076 Tübingen, Germany; [c]Graduate School of Neural Information Processing, University of Tübingen, 72074 Tübingen, Germany; [d]Network Imaging Group, Max Planck Institute for Biological Cybernetics, 72076 Tübingen, Germany; [e]Department of Behavior and Brain Organization, Center of Advanced European Studies and Research, 53175 Bonn, Germany; and [f]Digital Neuroanatomy, Max Planck Florida Institute, Jupiter, FL 33458

Contributed by Bert Sakmann, September 23, 2015 (sent for review April 22, 2015; reviewed by Heinz Beck, Fritjof Helmchen, and Bernardo Rudy)

Cortical inhibitory interneurons (INs) are subdivided into a variety of morphologically and functionally specialized cell types. How the respective specific properties translate into mechanisms that regulate sensory-evoked responses of pyramidal neurons (PNs) remains unknown. Here, we investigated how INs located in cortical layer 1 (L1) of rat barrel cortex affect whisker-evoked responses of L2 PNs. To do so we combined in vivo electrophysiology and morphological reconstructions with computational modeling. We show that whisker-evoked membrane depolarization in L2 PNs arises from highly specialized spatiotemporal synaptic input patterns. Temporally L1 INs and L2–5 PNs provide near synchronous synaptic input. Spatially synaptic contacts from L1 INs target distal apical tuft dendrites, whereas PNs primarily innervate basal and proximal apical dendrites. Simulations of such constrained synaptic input patterns predicted that inactivation of L1 INs increases trial-to-trial variability of whisker-evoked responses in L2 PNs. The in silico predictions were confirmed in vivo by L1-specific pharmacological manipulations. We present a mechanism—consistent with the theory of distal dendritic shunting—that can regulate the robustness of sensory-evoked responses in PNs without affecting response amplitude or latency.

layer 1 | barrel cortex | cortical column | shunting | NMDAR

Mechanistic understanding of the principles that underlie sensory-evoked neuronal responses remains a key challenge in neuroscience research. Although electrophysiological and optical imaging techniques provide access to activity patterns of individual and/or populations of neurons in live animals, information about the organization of the underlying synaptic input patterns that drive neuronal activity remains scarce. Here, we investigate the mechanisms underlying whisker deflection-evoked responses in pyramidal neurons (PNs) in the vibrissal part of rat primary somatosensory cortex (vS1, i.e., barrel cortex) (1). Specifically, we wanted to know whether and how L1 interneurons (INs) shape responses of L2 PNs. L1 is densely populated by apical tuft dendrites from multiple types of excitatory PNs and a sparse population of GABAergic INs (2). Recent studies in acute parasagittal (3) and coronal (4) brain slices in vitro have shown that L1 INs have axonal projections largely confined to L1, where they form synaptic connections with the dendrites from PNs located in L2/3 (5) and L5 (4). These connections place L1 INs in a perfect position to manipulate the activity of PNs, for example, by feed-forward inhibition and/or more indirect mechanisms such as disinhibition (4, 6). However, the influence of L1 INs on the sensory-evoked responses of PNs remains unclear.

To address this, we performed whole-cell patch-clamp recordings in vivo and reconstructed the 3D morphologies of the recorded L1 INs. These data, acquired under the same experimental conditions as previously used to determine whisker-evoked spiking and 3D morphologies for PN cell types (7), were used to inform and constrain simulation experiments. Specifically, we converted the 3D soma/dendrite morphology of an in vivo-labeled L2 PN into a biophysically detailed full-compartmental model (8) and integrated the neuron model into a recently reported detailed reconstruction of the excitatory circuitry in vS1 (9). This integration enabled us to statistically measure the number and subcellular distribution of cell type-specific synaptic contacts impinging onto the exemplary L2 PN from L1 INs and L2–5 PNs, respectively. These spatially constrained synaptic input patterns were further constrained temporally by using the measured cell type-specific spiking probabilities and latencies (7, 10). Finally, we made in silico experiments (i.e., numerical simulations) and investigated how the interplay between biophysical properties of the dendrites and well-constrained spatiotemporal synaptic input patterns give rise to the whisker-evoked responses measured in vivo (11).

Results

L1 INs Have Short Latency Whisker-Evoked Responses. Using two-photon (2p) microscopy (Fig. 1*A*), L1 INs in vS1 in anesthetized rats were targeted for whole-cell recordings ($n = 29$; soma depth from pia: 25–105 μm, mean ± SD: 59 ± 24 μm). Current injections in vivo resulted in heterogeneous patterns of action potential (AP) responses (Fig. 1*B*), which closely resembled those observed for L1 INs in acute brains slices in vitro (3–5). Next, after identification of the respective principal whisker [PW, using intrinsic optical imaging (IOI)], we measured spontaneous and whisker deflection-evoked

Significance

Even the simplest sensory stimulus activates millions of synapses across the cortex. How neurons integrate these highly specialized, but noisy synaptic input patterns to generate robust electrophysiological responses—that ultimately translate into behavior—remains elusive. Here, we provide first insight into a mechanism that may underlie the general phenomenon, observed across sensory modalities and species, that stimulation decreases variability in neuronal activity. Specifically, we show that during sensory stimulation, highly specialized inhibitory neurons provide synaptic input to distal dendrites of excitatory neurons, which reduces variability but not the mean amplitude of the response. Distal dendritic shunting may thus represent a general principle of cortex organization to ensure that noisy synaptic input patterns translate into robust sensory-evoked neuronal activity.

Author contributions: A.C.S., D.J.W., B.S., M.O., and J.N.D.K. designed research; R.E., A.C.S., D.J.W., M.O., and J.N.D.K. performed research; R.E., A.C.S., D.J.W., M.O., and J.N.D.K. analyzed data; and R.E., A.C.S., D.J.W., M.O., and J.N.D.K. wrote the paper.

Reviewers: H.B., University of Bonn; F.H., Universität Zürich; and B.R., NYU Langone Medical Center.

The authors declare no conflict of interest.

Freely available online through the PNAS open access option.

Data deposition: The model, including a detailed documentation of all parameters and the analysis routines, can be obtained from ModelDB, senselab.med.yale.edu/ModelDB/ (accession no. 167499).

[1]R.E. and A.C.S. contributed equally to this work.

[2]To whom correspondence may be addressed. Email: marcel.oberlaender@tuebingen.mpg.de or bert.sakmann@mpfi.org.

This article contains supporting information online at www.pnas.org/lookup/suppl/doi:10.1073/pnas.1518773112/-/DCSupplemental.

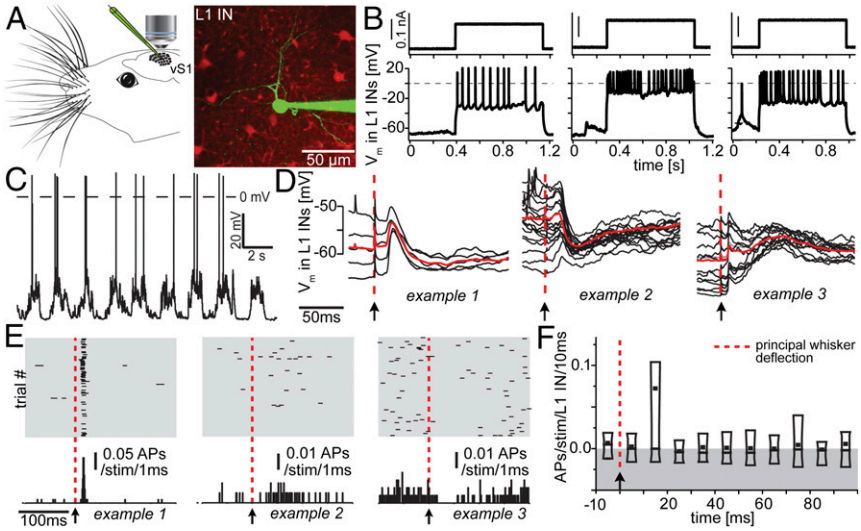

Fig. 1. Functional characterization of L1 INs recorded in vivo. (*A*) Individual L1 INs in rat vS1 were targeted for whole-cell recordings using 2p microscopy. (*B*) Step current injection-evoked spiking responses (three exemplary neurons are shown). (*C*) Ongoing up- and down-state activity of exemplary L1 IN. (*D*) All recorded L1 INs had short latency subthreshold responses following whisker deflections (three exemplary neurons are shown). Red, average across trials. (*E*) Whisker-evoked spiking of the neurons shown in *D*. (*F*) Poststimulus time histogram at 10-ms resolution of whisker-evoked spiking across all recorded L1 INs. Box, 10th–90th percentile; line, median; dot, mean.

sub- or suprathreshold responses for each recorded L1 IN. Spontaneous AP frequency was 1.1 ± 0.9 Hz (Fig. 1*C*). All recorded L1 INs displayed reliable whisker-evoked subthreshold responses (Fig. 1*D*) with onset latencies (9.8 ± 2.2 ms, for definition, see *Materials and Methods*) (12) as short as those previously reported for PN cell types in L3–5 (11, 13, 14). Fourteen of 29 L1 INs showed whisker-evoked APs. Although AP responses were heterogeneous (Fig. 1*E*), spiking occurred most strongly in the first 20 ms after stimulus, and when averaged for all neurons, the time window of 10–20 ms contained the majority of stimulus evoked APs. On average, AP responses had returned to prestimulus rates in less than 20 ms (average, 15.2 ± 2.2 ms; Fig. 1*F*). Within the 10- to 20-ms window, whisker-evoked activity across all L1 INs was 0.07 ± 0.23 APs per stimulus. Neither subthreshold nor AP responses were correlated with spontaneous AP frequencies (Fig. S1).

L1 IN Axons Innervate L1 of All Surrounding Columns. Following the in vivo recording, L1 INs were labeled with biocytin for post hoc reconstruction of 3D dendrite and axon morphologies. Additionally, outlines of the pial surface and L4 barrels were traced and used for registration of the morphologies into an accurate 3D reference frame of the vS1 geometry (15) (Fig. 2 *A* and *B*). All reconstructed L1 INs (n = 10; Fig. S2) displayed comparable dendritic fields and 3D axon projection patterns. In the horizontal plane (tangential to vS1; Fig. 2*A*), axonal projections spread beyond the dimensions of the principal column (PC, i.e., containing the soma), thus innervating all surrounding barrel columns (SCs; Fig. 2*C*). In the coronal plane, axons were confined to L1, with a subset of cells displaying additional sparse branches descending into L2/3 of the PC (Fig. 2*D*). Similar laminar axon patterns were observed in vitro and were used to subdivide L1 INs into axonal cell types [e.g., neurogliaform (NGF)-like INs] (4). However, criteria to distinguish between morphological types are ambiguous (3). Moreover, whether morphological properties correlate with electrophysiological responses remains controversial (3, 5). In our data, current injection-evoked responses in vivo were heterogeneous and did not correlate with dendritic and/or axonal properties (Fig. S2). Similarly, spontaneous AP frequencies and whisker-evoked responses across INs with axons confined to L1 were not significantly different from those that projected additional sparse branches to L2/3. Consequently, we grouped all L1 INs as one cell type for the present study.

Reverse Engineering Synaptic Input Patterns to L2 PNs. To investigate how feed-forward inhibition from L1-to-PN synaptic contacts could affect whisker-evoked responses, we integrated the reconstructed L1 INs into a statistical model of the neuronal networks in vS1 (9) (Fig. 3*A*). We selected one representative L2 PN from the model network, converted its soma and dendrites into a full-compartmental biophysical model (8), and determined the number and subcellular distribution of synaptic contacts it receives from seven axo-dendritic PN cell types (16) and L1 INs, respectively (Table S1). L1 IN inputs were located on distal apical dendrites and largely separated from those of L2–5 PNs (Fig. 3*B*). Based on the present data of AP firing in L1 INs, and previously reported measurements of response (7) and pairwise connection probabilities (17, 18) (Table S2) for the PN cell types, we determined the cell type-specific numbers of active synaptic contacts impinging onto the L2 model neuron before and during a whisker deflection (Fig. 3*C*).

This procedure was repeated 50 times by varying the presynaptic partner neurons assigned to each (or multiple) synaptic contacts, reflecting different configurations of anatomical connectivity in the model network. For each of these anatomical configurations, the identity and spike timing of active presynaptic neurons during the spontaneous and whisker-evoked epochs was then varied 2,000 times to represent different configurations of the functional connectivity in the network. Consequently, 100,000 L2 neuron models were generated with different spatiotemporal configurations of synaptic input, each model meeting the measured anatomical and functional constraints of the vS1 circuitry and the

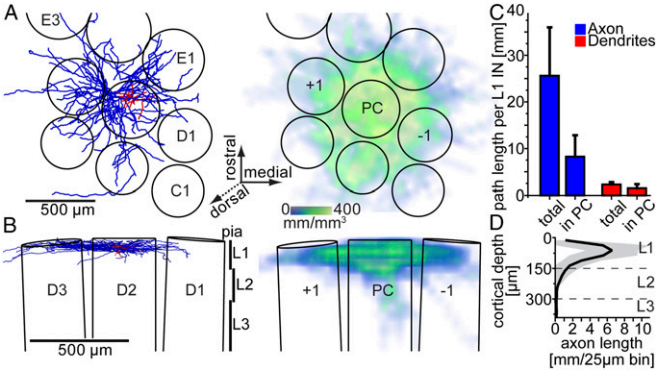

Fig. 2. Morphological characterization of L1 INs labeled in vivo. (*A*) (*Left*) Exemplary reconstruction of L1 IN (red, dendrites; blue, axon) registered to a 3D model of vS1 (top view onto the cortical surface). (*Right*) 3D axon density averaged across all reconstructed and registered L1 INs. (*B*) Coronal views of *A*. Axonal projections remained either confined to L1 (*Left*) or displayed additional sparse branches descending into L2 (*Right*). (*C*) Average path lengths per L1 IN within and outside the principal column (PC). (*D*) 1D axon length profile along the vertical cortex axis averaged across all L1 INs (black, mean; gray, SD).

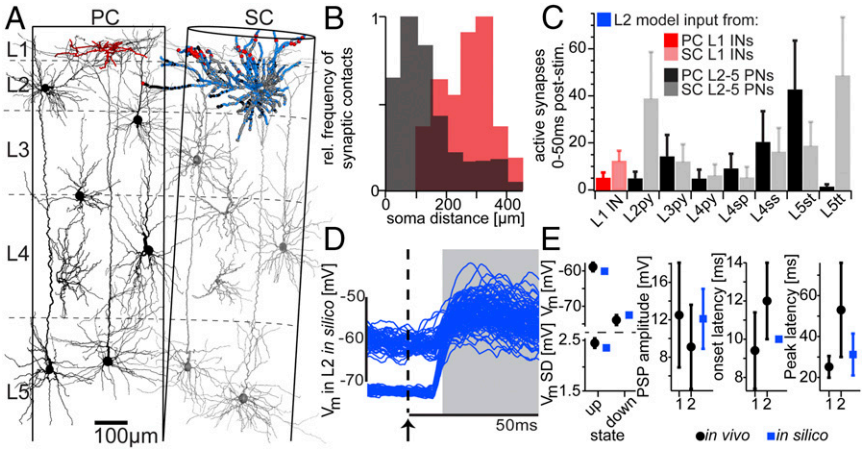

Fig. 3. Whisker-evoked responses in silico. (*A*) Full-compartmental model of an in vivo-labeled L2 PN (blue), embedded into an anatomically well-constrained model of the average vS1 circuitry (exemplary in vivo-labeled dendrites are shown for each PN cell type). The number and subcellular distribution of synaptic contacts impinging onto the L2 model were determined statistically (1% of the synaptic contacts for one of 50 models are shown). (*B*) Path length distances between synaptic contacts from PC L2-5 PNs (black) and PC L1 INs (red) and the soma of the L2 model. (*C*) Cell type-specific number of active synaptic contacts during a period of 50 ms following whisker deflection. (*D*) Simulation of 200 trials of ongoing and whisker-evoked synaptic activity using the model configuration shown in *A* (15 ms of ongoing activity before and 50 ms of evoked activity after the whisker deflection stimulus are shown). (*E*) Comparison between simulated (in silico) and in vivo measured ongoing (8) or whisker-evoked PSPs. 1 and 2 refer to L2 PSP measurements in the present (Fig. 5) and a previous study (11), respectively.

present experimental in vivo conditions, respectively. Finally, using the compartmental model neuron described above, we simulated dendritic integration of the spatiotemporal synaptic input patterns to generate simulated membrane potential traces (Fig. 3*D*). The in silico somatic membrane potential activity (Table S3) displayed ongoing up and down state activity comparable in time course and amplitude to previous in vivo measurements (8), as well as recorded membrane activity in the current study. Similarly, the shape of the postsynaptic potentials (PSPs) in silico (i.e., peak amplitude, onset, and peak latencies) were comparable with those of the present and previous (11) in vivo measurements (Fig. 3*E*).

In Silico Prediction: L1 INs Regulate PSP Robustness. To test the impact of distal L1-to-L2 synaptic inputs onto the whisker-evoked PSPs, we repeated the simulations, but deactivated the L1 INs in the PC (Fig. 4*A*). We found that the variability of whisker-evoked PSPs (SD of membrane depolarization 15–50 ms after stimulus across trials) increased significantly (Fig. 4*B*), whereas the shape of the mean PSP remained largely unchanged (Fig. S3*A*). To determine a possible mechanism underlying this in silico prediction, we performed sensitivity analyses by repeating the simulations, but systematically varying one of the anatomical, functional, and biophysical parameters within the measured constraints while keeping the other parameters unchanged (Fig. 4*C*). First, we found that varying functional connectivity of PNs did not influence average trial-to-trial variability. In contrast, leaving functional configurations of PNs unchanged and deactivating L1 INs, the simulations resulted in identical increases of trial-to-trial variability for each of the 50 anatomical connectivity configurations. Next, hyperpolarizing the chloride reversal potential (Fig. S3*B*) or increasing the strength of the L1 IN synapses beyond the value used for all simulations did not change the effect on trial-to-trial variability. The latter is in line with a previous study, which showed that changes in input resistance saturate for large conductance values (19). Finally, by removing the NMDA receptor (NMDAR) conductances, the increase in trial-to-trial variability was largely abolished. Taken together, the observed change in trial-to-trial variability critically depends on the location (not strength) of the L1 IN inputs and the presence of NMDAR conductances.

These results are reminiscent of theoretical work (20), which suggested that IN inputs can affect NMDAR conductances locally and/or globally, depending on the relative locations of the excitatory and inhibitory synapses (Fig. S4 *A* and *B*). First, IN input hyperpolarizes the membrane potential, which results in shunting of the adjacent (i.e., as determined by the passive membrane properties) dendritic compartments. Activation of NMDAR conductances within the shunted compartments will thus generate smaller depolarization, compared with nonshunted dendrites ("local" effect). Second, the local shunting also suppresses NMDAR-mediated nonlinearities [note that in this model nonlinearities are solely determined by the voltage-dependent activation of the NMDAR conductance due to the magnesium block (20, 21)], which effectively decreases regenerative dendritic events, also at locations that are not directly affected by the shunting ("global" effect). Thus, in case IN inputs are activated simultaneously with PN inputs (e.g., after whisker deflection), the average (i.e., across trials) evoked membrane potential within shunted dendritic compartments should be smaller compared with situations with no IN input (ΔV_m). At the same time, NMDAR-mediated nonlinearities should be reduced throughout the entire dendritic tree, which can be quantified as the change (with vs. without IN input) of the trial-to-trial variability (ΔSD) of the membrane potential. We quantified the two effects by calculating the "shunt level" (SL) (20) along the dendrites of our L2 PN model (Fig. 4*D*). The SL decreased monotonically from the distal location of highest L1 IN input density, reaching zero ∼100 µm from the soma. As predicted by the theory, ΔV_m was proportional to the SL (Pearson correlation coefficient $R = 0.62$, $P = 0.02$), and hence decreased monotonically toward the soma (Fig. 4*E*). In contrast, ΔSD was independent of the dendritic location and the respective SL ($R = –0.02$, $P = 0.95$). To confirm that the decoupling between ΔSD and the SL was indeed caused by suppression of regenerative nonlinear events, we removed the NMDAR conductances from the model. Then, ΔV_m and ΔSD decreased both monotonically toward the soma (i.e., proportional to the SL; Fig. 4*E*).

In Vivo Pharmacology Confirms in Silico Predictions. To test the in silico predictions, we designed in vivo experiments that closely resembled the conditions of the model (Fig. 5*A*). Specifically, we injected an AMPAR-specific antagonist (GYKI-53655; Ivax) locally into L1 of the PC to prevent L1 INs from AP firing (Fig. 5*B*). To validate that this pharmacological manipulation remained specific to L1 INs, we imaged somatic calcium transients in populations of L2/3 neurons, right below the injection site, before and during the injection of GYKI. Neither the average whisker-evoked population response in L2/3 ($n = 42$ neurons from three animals: $P = 0.79$, $P = 0.17$, and $P = 0.29$) nor its variability was significantly changed (Fig. 5*C*). To validate that the injection procedure itself did not alter the subthreshold whisker-evoked responses of L2 PN, we

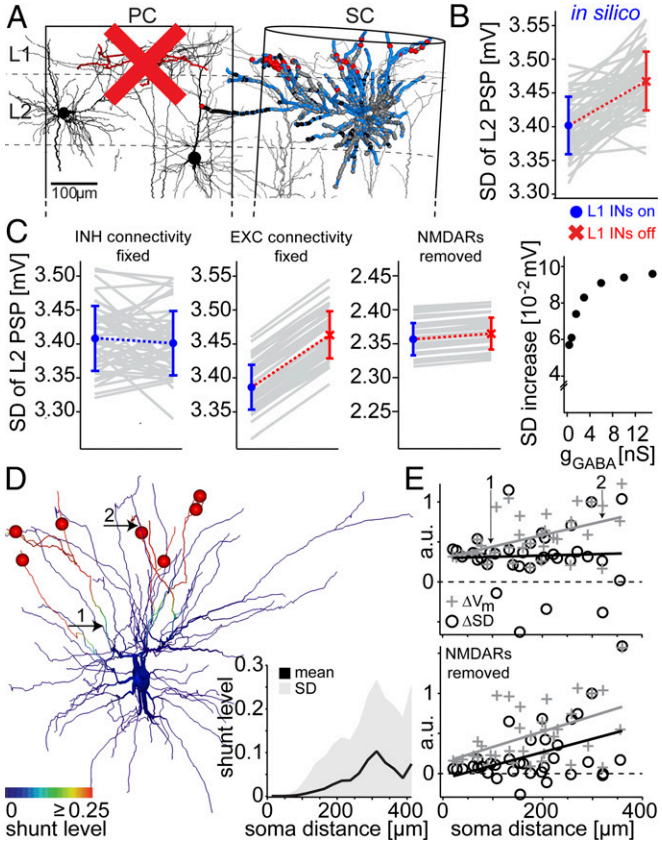

Fig. 4. Deactivation of L1 INs in silico predicts increase of L2 PSP variability. (*A*) The same model configuration as in Fig. 3, but without L1 INs in the PC. (*B*) Comparison of whisker-evoked PSP variability between models with (*Left*) and without (*Right*) PC L1 INs (each gray line refers to one of the 50 anatomical models). (*C*) Sensitivity analyses from left to right: varying functional connectivity of PN synaptic contacts; keeping PN functional connectivity fixed and deactivating PC L1 INs; removing NMDARs from PN synapses; varying L1 IN synapse strengths around the value used in all simulations (1.6 nS). (*D*) L1 IN inputs shunt dendritic branches as quantified by the shunt level (SL). The average (across trials) SL decreases monotonically toward proximal dendrites, reaching zero ∼100 µm from the soma. (*E*) Change (with vs. without L1 INs) of the average (across trials) membrane potential (ΔV_m) and its variability (ΔSD), calculated at multiple dendritic locations in the presence (*Upper*) and absence (*Lower*) of NMDARs in the model.

made whole-cell recordings and measured L2 PSPs in response to PW deflection before and during injection of saline into L1 ($n = 5$, $P = 0.63$; Fig. 5*D*). Based on these control experiments, we could investigate how the absence of L1 INs affects whisker-evoked PSPs in L2 PNs in vivo. To do so, we made whole-cell recordings on L2 PNs (located within a SC) and measured PSPs in response to PW deflection before and during the injection of GYKI into L1 of the PC. Remarkably, every L2 PN recorded under these experimental settings ($n = 7$) showed an increase in trial-to-trial variability (4.0 ± 1.4 vs. 4.7 ± 1.7 mV; $P = 0.02$; Fig. 5*E*). In contrast, the shape of the PSP response remained unchanged, with neither membrane potentials at peak amplitudes (−51.9 ± 6.1 vs. −51.8 ± 7.1 mV; $P = 1$) nor peak latencies (25.2 ± 5.3 vs. 26.6 ± 5.9 ms; $P = 0.16$) being significantly altered (Fig. 5*F*).

Discussion

Whisker-Evoked Synaptic Input Patterns to L2 PNs. In the present study, we looked at the functional contribution of L1 INs on whisker-evoked subthreshold membrane responses using a combination of in vivo data and modeling. Using this combination, we estimated the synaptic inputs impinging onto L2 PNs in rat vS1. We generated synaptic input maps by calculating the structural overlap between the dendrites of a representative L2 PN morphology and a dense statistical model of the cell type-specific axon/bouton distributions in rat vS1 (9). The number of synaptic contacts was further multiplied with in vivo-recorded AP probabilities of the respective PN cell types (7). This procedure estimated that the model neuron received on average 3 ± 1 excitatory synaptic inputs per millisecond during simulated periods of ongoing activity (i.e., up-states). Previously, the same number of active synaptic contacts was estimated by tuning activity of presynaptic neurons until voltage traces simulated within a full-compartmental model met those obtained by whole-cell recordings during up-states in vivo (8).

Our data further suggest that these excitatory inputs originate from a highly heterogeneous mix of PNs located throughout all cortical layers of the PC and SCs. Consequently, our results contradict the classical view of the cortical circuitry, which postulated L4 as the primary source of feed-forward excitation in L2/3. This view had been challenged previously, where high-resolution 2p imaging of Ca^{2+} hotspots (i.e., putative spines) on dendrites of L2 PNs in mouse vS1 (22) revealed that the majority of spines responded to deflections of the PW and SWs. In line with these in vivo imaging results, we estimate that ∼50% of the excitatory inputs (primarily from L5) to L2 PNs can be activated by the PW and SWs, 30% and 20% (primarily from L2–4) exclusively by the PW or by a SW, respectively. Our approach hence provides a quantitative insight into the presynaptic populations that give rise to the salt-and-pepper-like distributions of PW and SW specific, as well as of nonspecific excitatory inputs to L2 PNs.

Distal Dendritic Shunting. Our simulations showed that the separation between IN and PN inputs along the dendrites, the distance between the IN inputs and the soma, the relative timing of IN and PN inputs, and the number of active IN inputs (Fig. S3*A*) determine the degree by which the local (change in V_m) and global (change in SD of V_m) effects of shunting are observable at the soma. In case of the present model, L1-induced shunting does not reach the soma (Fig. S4*C*). In turn, we estimated that nonlinear, global (i.e., visible at the soma) events increase by ∼15% if L1 INs are absent (Fig. S4*D*). As a result, whisker-evoked L1 IN inputs do not affect the amplitude of the average somatic PSP in L2 PNs, but stabilize this response across trials. Further evidence suggesting that our model captures the general organizational principles of the L1 to L2 pathway arises from the pharmacological experiments. If L1 IN inputs would be located closer to the soma, the shunting will also affect more proximal dendritic compartments, including the soma. Consequently, both the amplitude of the somatic PSP and its variability should decrease in the absence of L1 INs (Fig. S3) (23): an effect we did not observe during blockage of L1 INs in vivo.

Distal dendritic shunting may be regarded as an elegant mechanism to decouple one of the advantages of voltage-dependent dendritic nonlinearities, amplification of PN input, from one of its major disadvantages, amplification of trial-to-trial variability. Although the nonlinearities may originate from various mechanisms (6, 20, 24), and their respective impacts may depend on the animal's behavioral state (25), segregation of proximal PN from distal IN inputs may be a general organizational principle of the cortex to specifically control the robustness of sensory-evoked responses. Churchland et al. (26) demonstrated that sensory stimulation—independent of the sensory modality, specifics of the stimulus, cortical area, or species—always results in significant decreases of variability, both for subthreshold and AP responses. We propose a general mechanism that may underlie this observation. First, INs in L1 receive relatively little input from intrinsic (i.e., within the same cortical area) excitatory pathways. Second, L1 is innervated by long-range pathways from multiple cortical (27) and thalamic areas (e.g., posterior medial division of the thalamus (POm) (28)), as well as from neuromodulatory pathways (29). We therefore suggest that L1 INs are primarily driven by nonspecific long-range pathways, for example as previously demonstrated by neurons in the contralateral hemisphere (6) or by thalamic nuclei (30). In line with this

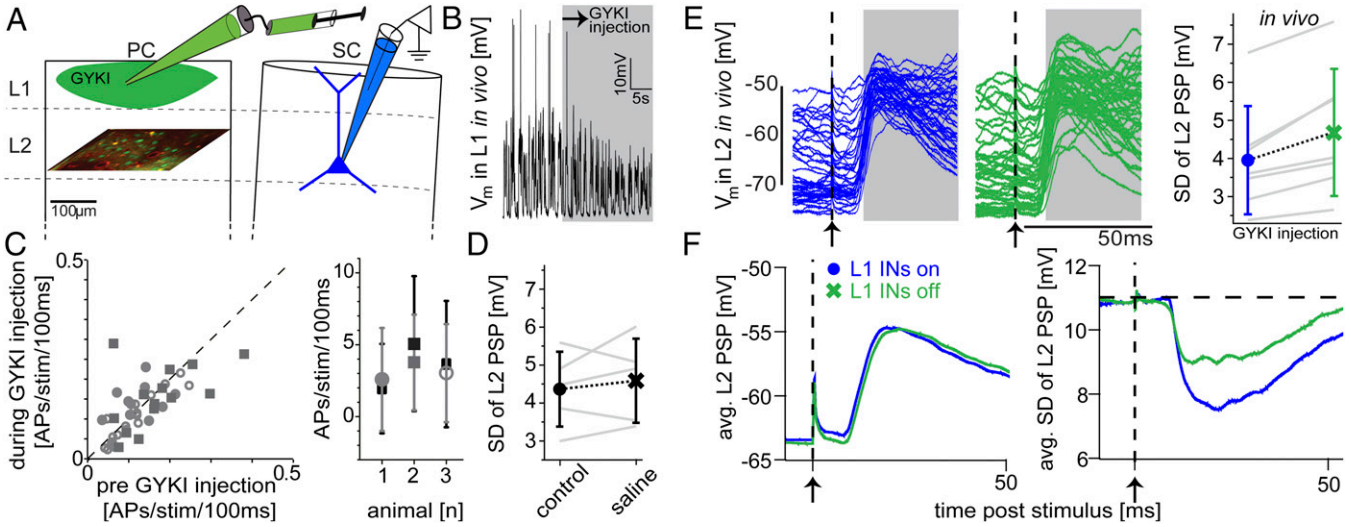

Fig. 5. Pharmacological deactivation of L1 INs in vivo confirms in silico predictions. (*A*) Experimental setting to match in vivo conditions with the in silico scenario shown in Fig. 4. Whole-cell patch-clamp recordings were performed on L2 PNs located in a SC during deflections of the PW before and during injection of GYKI locally into L1 of the PC to prevent spiking in L1 INs. (*B*) Whole-cell recording showing ongoing activity of exemplary L1 IN located within the PC before and during GYKI injection. (*C*, *Left*) Whisker-evoked response probabilities of L2 neurons within the PC, as revealed by 2p calcium imaging, before and during the injection of GYKI. (*Right*) Whisker-evoked APs in PC L2 neurons in the same animal before (black) and during (gray) GYKI injections. (*D*) PC L1 injections of saline had no systematic effect on L2 PSP variability. (*E*) Ongoing and whisker-evoked subthreshold activity of exemplary L2 PN before (*Left*) and during (*Center*) pharmacological blockage of L1 INs. (*Right*) Variability across whisker deflection trials of PSP response increased for every recorded L2 PN. (*F*) Average PSP (*Left*) and trial-to-trial variability (*Right*) across all L2 PNs before (blue) and during (green) GYKI injections.

suggestion is our observation that whisker-evoked APs of L1 INs were largely unaffected by recurrent excitation in the underlying layers (10). As a result, L1 INs could effectively control the robustness of sensory-evoked responses in PNs, independent of the specifics of the stimulus.

However, distal shunting by L1 INs is not sufficient to explain the general phenomenon of stimulus-evoked stabilization. For example, PNs in L6 do not project their dendrites to L1 (7), and shunting of apical tuft dendrites of L5 PNs will in general not affect dendrites all of the way to the soma (31). We therefore suggest that INs at the L4/5 border serve a similar function for controlling the robustness of PNs in L5 and L6. In support of this suggestion, apical tuft dendrites of L6 PNs terminate at the L4/5 border (32), which is also the location where unspecific projections from POm densely innervate the cortex (28) and where NGF-like INs with axon morphologies similar to L1 INs are frequently found (33). Distal dendritic shunting via NGF-like INs in L1 and L4/5 may thus represent a general organizational principle of the cortical circuitry to ensure that sensory stimuli evoke robust feed-forward responses in PNs (Fig. S5).

Materials and Methods

Animal Preparation. All experimental procedures were carried out according to the animal welfare guidelines of the Max Planck Society. Wistar rats (m/f, P25–35, 80–140 g) were anesthetized with urethane (i.p.; 1.6–2 g/kg body weight). The animal's skull was exposed and cleaned, and a metal plate was attached with dental acrylic cement. A 2- to 3-mm-wide craniotomy was opened above vS1 centered on bregma −2.5 mm and lateral 5.5 mm. The exposed cortex was superfused with warm normal rat Ringer (NRR) solution. The craniotomy was filled with agarose and covered with an immobilized glass coverslip.

Imaging of Intrinsic Optical Signals. Functional maps of vS1 were determined using IOI (34). The cortical surface was illuminated with red light (630 nm) while stimulating a single whisker (10 deflections of 1–2° amplitude in the ventral-dorsal direction at 5 Hz). Reflectance images were acquired at 10-Hz frame rate and averaged over 20–60 trials, which generated a spot roughly the size of a single barrel column. The surface blood vessel pattern was imaged for reference using green illumination (546 nm).

Fluorescence Labeling and Two-Photon Imaging. 2p imaging was performed using a custom-built 2p laser-scanning microscope (excitation wavelength, 872 nm; laser model Mai Tai HP; Spectra-Physics). Multicell bolus loading of neocortical cells with the calcium indicator Oregon Green BAPTA [1,2-bis(2-aminophenoxy)ethane-N,N,N′,N′-tetraacetic acid]-1 (OGB-1) AM (Invitrogen) was performed in L2/3 as described before (35). Fluorescence Images of 64 × 128 pixels were acquired through a 20× water-immersion objective lens (0.95NA; Olympus).

Electrophysiology. Unlabeled INs located in L1 and PNs in L2 of rat vS1 were targeted for whole-cell electrical recordings using 2p microscopy. Recordings were targeted to the PC/SC using IOI. Open pipette resistance was 5–7 MΩ. Pipettes were filled with (in mM) K-gluconate 135, 4-(2-hydroxyethyl)-1-piperazineethanesulfonate (Hepes) 10, phosphocreatine-Na 10, KCl 4, ATP-Mg 4, GTP-Mg 0.3, and 0.3–0.5% biocytin. Fluorescent dye Alexa Fluor 594 (25–50 µM) or OGB-1 (100 µM) was added to visualize the pipette and the patched neurons. Membrane potential was recorded using an Axoclamp 2-B amplifier or a MultiClamp 700B amplifier (Axon Instruments) and digitized using a CED power1401 data acquisition board (CED; Cambridge Electronic Design).

Whisker Stimulation. A piezoelectric stimulator was attached to a whisker ∼10 mm from its base, and the whisker was deflected ∼5° (∼1-mm amplitude) for 500 ms. Stimulation was repeated at constant intervals of 2–3.5 s, was not triggered by membrane potential, and occurred randomly with respect to up- and down-states.

In Vivo Pharmacology. The specific antagonist for AMPA-type glutamate receptor 1-(4-aminophenyl)-3-methylcarbamyl-4-methyl-3,4,-dihydro-7,8-methylenedioxy-5H-2,3-benzodiazepine (GYKI-53655; Ivax) was injected to L1 of the PC to locally block postsynaptic activity (35). GYKI-53653 was diluted to 0.5 mM in NRR with an additional 15 mM Hepes. Alexa Fluor 594 (50–100 µM), Alexa Fluor 488, or OGB-1 (100 µM) was added to visualize the injected solution. Patch-clamp pipettes with a tip opening diameter of ∼2 µm were used for drug application. GYKI-53655 was injected at 50–120 mbar for 2 min.

Histology and Reconstruction. Rats were perfused transcardially with phosphate buffer followed by 4% (wt/vol) paraformaldehyde. The cortex was cut tangentially to vS1 (45°) in 100-µm-thick sections and stained for cytochrome oxidase and biocytin (Vectastain ABC-kit). Neuronal morphologies, as well as outlines of the pia and L4 barrels, were reconstructed using a brightfield microscope (Zeiss; Imager.Z1) attached to a Neurolucida system (Microbrightfield). Boutons along L1 IN axons had a mean distance of 2.6 ± 1.1 µm

(i.e., bouton density: 0.39 per μm axon, $n = 275$ measurements on $n = 5$ axon branches of $n = 3$ neurons).

Data Analysis. Membrane potential recordings were analyzed using custom written Matlab routines. Average excitatory postsynaptic potential (EPSP)/inhibitory postsynaptic potential (IPSP) amplitudes in a 100-ms window after stimulus onset were measured at the peak/trough of the membrane potential, relative to the average membrane potential in a 10-ms window before stimulus onset. Onset latency was defined as the time from stimulus onset to 10% of the EPSP/IPSP amplitude. Peak latency was defined as the time from stimulus onset to the membrane potential peak/trough. For spike detection, data were differentiated and thresholded at 1 mV/ms. Average spontaneous AP rate was calculated over a 1-s window before the stimulus (20–450 trials per neuron). For analysis of the subthreshold membrane potential time course, trials with spikes occurring within 150 ms after stimulation were excluded to prevent corruption of the time course by APs and afterhyperpolarization. The time window to determine the impact of L1 IN inputs on the whisker-evoked membrane potential of L2 PNs was chosen from 15 ms (i.e., average onset latency of L1 IN spiking) to 50 ms (i.e., because of the 20-ms decay time constant of the $GABA_A$ conductance). All error bars represent mean ± SD.

Statistical Testing. Statistical testing was performed using an unpaired two-sided *t* test. For GYKI and saline injection experiments, the nonparametric Wilcoxon rank-sum test was used. For both tests, the significance levels were set to 0.05.

Simulations. A detailed description of the model is provided in the *SI Materials and Methods*, and the model can be obtained from ModelDB (senselab.med.yale.edu/ModelDB/; accession no. 167499). Numerical simulations were carried out using the NEURON (36) package. A total of 2,000 simulation trials (1,000 for up- and down-states, respectively) were sufficient to minimize systematic errors (caused by undersampling the parameter spaces of functional connectivity configurations) to 2×10^{-3} mV.

ACKNOWLEDGMENTS. Funding was provided by the Max Planck Institute for Biological Cybernetics (R.E., A.C.S., D.J.W., M.O., and J.N.D.K.), Center for Advanced European Studies and Research (Caesar) (D.J.W. and J.N.D.K.), the Studienstiftung des deutschen Volkes (R.E.), the Bernstein Center for Computational Neuroscience, funded by German Federal Ministry of Education and Research Grant BMBF/FKZ 01GQ1002 (R.E. and M.O.), the European Research Council under the European Union's Horizon 2020 Research and Innovation Program (Grant Agreement 633428, to M.O.), and the Max Planck Florida Institute for Neuroscience (B.S. and M.O.).

1. Woolsey TA, Van der Loos H (1970) The structural organization of layer IV in the somatosensory region (SI) of mouse cerebral cortex. The description of a cortical field composed of discrete cytoarchitectonic units. *Brain Res* 17(2):205–242.
2. Marin-Padilla M, Marin-Padilla TM (1982) Origin, prenatal development and structural organization of layer I of the human cerebral (motor) cortex. A Golgi study. *Anat Embryol (Berl)* 164(2):161–206.
3. Muralidhar S, Wang Y, Markram H (2013) Synaptic and cellular organization of layer 1 of the developing rat somatosensory cortex. *Front Neuroanat* 7:52.
4. Jiang X, Wang G, Lee AJ, Stornetta RL, Zhu JJ (2013) The organization of two new cortical interneuronal circuits. *Nat Neurosci* 16(2):210–218.
5. Wozny C, Williams SR (2011) Specificity of synaptic connectivity between layer 1 inhibitory interneurons and layer 2/3 pyramidal neurons in the rat neocortex. *Cereb Cortex* 21(8):1818–1826.
6. Palmer LM, et al. (2012) The cellular basis of GABA(B)-mediated interhemispheric inhibition. *Science* 335(6071):989–993.
7. Oberlaender M, et al. (2012) Cell type-specific three-dimensional structure of thalamocortical circuits in a column of rat vibrissal cortex. *Cereb Cortex* 22(10):2375–2391.
8. Waters J, Helmchen F (2006) Background synaptic activity is sparse in neocortex. *J Neurosci* 26(32):8267–8277.
9. Egger R, Dercksen VJ, Udvary D, Hege HC, Oberlaender M (2014) Generation of dense statistical connectomes from sparse morphological data. *Front Neuroanat* 8:129.
10. de Kock CP, Bruno RM, Spors H, Sakmann B (2007) Layer- and cell-type-specific suprathreshold stimulus representation in rat primary somatosensory cortex. *J Physiol* 581(Pt 1):139–154.
11. Brecht M, Roth A, Sakmann B (2003) Dynamic receptive fields of reconstructed pyramidal cells in layers 3 and 2 of rat somatosensory barrel cortex. *J Physiol* 553(Pt 1):243–265.
12. Zhu Y, Zhu JJ (2004) Rapid arrival and integration of ascending sensory information in layer 1 nonpyramidal neurons and tuft dendrites of layer 5 pyramidal neurons of the neocortex. *J Neurosci* 24(6):1272–1279.
13. Brecht M, Sakmann B (2002) Dynamic representation of whisker deflection by synaptic potentials in spiny stellate and pyramidal cells in the barrels and septa of layer 4 rat somatosensory cortex. *J Physiol* 543(Pt 1):49–70.
14. Manns ID, Sakmann B, Brecht M (2004) Sub- and suprathreshold receptive field properties of pyramidal neurones in layers 5A and 5B of rat somatosensory barrel cortex. *J Physiol* 556(Pt 2):601–622.
15. Egger R, Narayanan RT, Helmstaedter M, de Kock CP, Oberlaender M (2012) 3D reconstruction and standardization of the rat vibrissal cortex for precise registration of single neuron morphology. *PLOS Comput Biol* 8(12):e1002837.
16. Narayanan RT, et al. (2015) Beyond columnar organization: Cell type- and target layer-specific principles of horizontal axon projection patterns in rat vibrissal cortex [published online ahead of print April 1, 2015]. *Cereb Cortex*, 10.1093/cercor/bhv053.
17. Feldmeyer D, Lübke J, Sakmann B (2006) Efficacy and connectivity of intracolumnar pairs of layer 2/3 pyramidal cells in the barrel cortex of juvenile rats. *J Physiol* 575(Pt 2):583–602.
18. Feldmeyer D, Lübke J, Silver RA, Sakmann B (2002) Synaptic connections between layer 4 spiny neurone-layer 2/3 pyramidal cell pairs in juvenile rat barrel cortex: Physiology and anatomy of interlaminar signalling within a cortical column. *J Physiol* 538(Pt 3):803–822.
19. Koch C, Douglas R, Wehmeier U (1990) Visibility of synaptically induced conductance changes: Theory and simulations of anatomically characterized cortical pyramidal cells. *J Neurosci* 10(6):1728–1744.
20. Gidon A, Segev I (2012) Principles governing the operation of synaptic inhibition in dendrites. *Neuron* 75(2):330–341.
21. Jahr CE, Stevens CF (1990) Voltage dependence of NMDA-activated macroscopic conductances predicted by single-channel kinetics. *J Neurosci* 10(9):3178–3182.
22. Varga Z, Jia H, Sakmann B, Konnerth A (2011) Dendritic coding of multiple sensory inputs in single cortical neurons in vivo. *Proc Natl Acad Sci USA* 108(37):15420–15425.
23. Hoffmann JH, et al. (2015) Synaptic conductance estimates of the connection between local inhibitor interneurons and pyramidal neurons in layer 2/3 of a cortical column [published online ahead of print March 10, 2015]. *Cereb Cortex*, 10.1093/cercor/bhv039.
24. Smith SL, Smith IT, Branco T, Häusser M (2013) Dendritic spikes enhance stimulus selectivity in cortical neurons in vivo. *Nature* 503(7474):115–120.
25. Sheffield ME, Dombeck DA (2015) Calcium transient prevalence across the dendritic arbour predicts place field properties. *Nature* 517(7533):200–204.
26. Churchland MM, et al. (2010) Stimulus onset quenches neural variability: A widespread cortical phenomenon. *Nat Neurosci* 13(3):369–378.
27. Mao T, et al. (2011) Long-range neuronal circuits underlying the interaction between sensory and motor cortex. *Neuron* 72(1):111–123.
28. Wimmer VC, Bruno RM, de Kock CP, Kuner T, Sakmann B (2010) Dimensions of a projection column and architecture of VPM and POm axons in rat vibrissal cortex. *Cereb Cortex* 20(10):2265–2276.
29. Poorthuis RB, Enke L, Letzkus JJ (2014) Cholinergic circuit modulation through differential recruitment of neocortical interneuron types during behaviour. *J Physiol* 592(Pt 19):4155–4164.
30. Cruikshank SJ, et al. (2012) Thalamic control of layer 1 circuits in prefrontal cortex. *J Neurosci* 32(49):17813–17823.
31. Larkum ME, Nevian T, Sandler M, Polsky A, Schiller J (2009) Synaptic integration in tuft dendrites of layer 5 pyramidal neurons: A new unifying principle. *Science* 325(5941):756–760.
32. Narayanan RT, et al. (2015) Beyond cortical columns: Cortex is organized by cell type- and target layer-specific horizontal axons. *Cereb Cortex* 25(11):4450–4468.
33. Koelbl C, Helmstaedter M, Lübke J, Feldmeyer D (2015) A barrel-related interneuron in layer 4 of rat somatosensory cortex with a high intrabarrel connectivity. *Cereb Cortex* 25(3):713–725.
34. Grinvald A, Lieke E, Frostig RD, Gilbert CD, Wiesel TN (1986) Functional architecture of cortex revealed by optical imaging of intrinsic signals. *Nature* 324(6095):361–364.
35. Kerr JN, Greenberg D, Helmchen F (2005) Imaging input and output of neocortical networks in vivo. *Proc Natl Acad Sci USA* 102(39):14063–14068.
36. Hines ML, Carnevale NT (1997) The NEURON simulation environment. *Neural Comput* 9(6):1179–1209.
37. Meyer HS, et al. (2013) Cellular organization of cortical barrel columns is whisker-specific. *Proc Natl Acad Sci USA* 110(47):19113–19118.
38. Holmes WR, Rall W (1992) Electrotonic length estimates in neurons with dendritic tapering or somatic shunt. *J Neurophysiol* 68(4):1421–1437.
39. Sachdev RN, Ebner FF, Wilson CJ (2004) Effect of subthreshold up and down states on the whisker-evoked response in somatosensory cortex. *J Neurophysiol* 92(6):3511–3521.
40. Lavzin M, Rapoport S, Polsky A, Garion L, Schiller J (2012) Nonlinear dendritic processing determines angular tuning of barrel cortex neurons in vivo. *Nature* 490(7420):397–401.
41. Hay E, Segev I (2015) Dendritic excitability and gain control in recurrent cortical microcircuits. *Cereb Cortex* 25(10):3561–3571.